PNAS RESEARCH ARTICLE | EARTH, ATMOSPHERIC, AND PLANETARY SCIENCES

On the identification of hyperhydrated sodium chloride hydrates, stable at icy moon conditions

Baptiste Journaux[a,1], Anna Pakhomova[b,c], Ines E. Collings[c,d], Sylvain Petitgirard[e], Tiziana Boffa Ballaran[f], J. Michael Brown[a], Steven D. Vance[g], Stella Chariton[h], Vitali B. Prakapenka[h], Dongyang Huang[e], Jason Ott[a], Konstantin Glazyrin[b], Gaston Garbarino[c], Davide Comboni[c], and Michael Hanfland[c]

Edited by Joanna Aizenberg, Harvard University, Cambridge, MA; received October 7, 2022; accepted January 20, 2023

Sodium chloride is expected to be found on many of the surfaces of icy moons like Europa and Ganymede. However, spectral identification remains elusive as the known NaCl-bearing phases cannot match current observations, which require higher number of water of hydration. Working at relevant conditions for icy worlds, we report the characterization of three "hyperhydrated" sodium chloride (SC) hydrates, and refined two crystal structures [$2NaCl{\cdot}17H_2O$ (SC8.5); $NaCl{\cdot}13H_2O$ (SC13)]. We found that the dissociation of Na^+ and Cl^- ions within these crystal lattices allows for the high incorporation of water molecules and thus explain their hyperhydration. This finding suggests that a great diversity of hyperhydrated crystalline phases of common salts might be found at similar conditions. Thermodynamic constraints indicate that SC8.5 is stable at room pressure below 235 K, and it could be the most abundant NaCl hydrate on icy moon surfaces like Europa, Titan, Ganymede, Callisto, Enceladus, or Ceres. The finding of these hyperhydrated structures represents a major update to the H_2O–NaCl phase diagram. These hyperhydrated structures provide an explanation for the mismatch between the remote observations of the surface of Europa and Ganymede and previously available data on NaCl solids. It also underlines the urgent need for mineralogical exploration and spectral data on hyperhydrates at relevant conditions to help future icy world exploration by space missions.

sodium chloride | hydrates | icy moons | Europa | Ganymede

Significance

The finding of sodium chloride hydrate phases allows an update to the phase diagram of the canonical H_2O–NaCl binary system in over 150 y. These phases identified at low temperatures and over a large range of pressures have hyperhydrated structures (ions dissociated within the lattice). This suggests that a great diversity of hyperhydrated crystalline phases of common salts might be found at similar conditions. This finding offers an explanation for the long-standing mystery of the unidentified hydrate at the surface of icy moons and allows to better understand their oceans and their potential for habitability.

Sodium chloride is the prototype for ionic solids and aqueous electrolytes. Abundant in terrestrial oceans, geofluids, and in organisms, the H_2O–NaCl system serves as the reference binary system in thermodynamics, physical chemistry, geosciences, medicine, and in engineering applications (1–4). This system, including both solid and solution phases, has been extensively studied as a function of temperature near-ambient pressures and to high pressures at higher temperatures because of its role in deep geological fluids (2, 3). While the vast majority of studies of stable solid phases in this system have focused on more Earth-like conditions above 250 K, there is a growing interest to explore lower temperatures (<250 K) and elevated pressures (>50 MPa) with the discovery of deep and salty extraterrestrial oceans in icy moons of Jupiter and Saturn (5, 6). As new space missions are set to geophysically investigate the icy crust and the deep liquid oceans in icy moons of our solar system—European Space Agency JUpiter ICy moons Explorer (JUICE), NASA's Europa Clipper and Dragonfly (7–9)—there is a critical need to accurately characterize relevant aqueous systems, notably H_2O–NaCl, at high pressures and below 300 K.

Sodium chloride dihydrate, the mineral hydrohalite, $NaCl{\cdot}2H_2O$ (SC2), space group $P2_1/c$ (10) is the only previously identified solid hydrate phase of NaCl. The only reported high-pressure liquidus measurements for NaCl, hydrohalite and ice polymorphs are at 298 K up to 1,400 MPa (11), and up to 400 MPa and down to 260 K (12). Valenti et al. (13) noted a possible new H_2O–NaCl phase, described as "columnar" in habit, between 200 and 1,200 MPa. This phase had a unique Raman spectrum characterized by three bands at 3,410, 3,460, and 3,510 cm^{-1}, which are not attributable to hydrohalite or other high-pressure ices at these conditions. However, the structure and physical characteristics of this phase were not determined and demonstrate the variety and complexity of the system.

NaCl is anticipated to be a major solute in extraterrestrial oceans (14), based on i) geochemical modeling of their formation (5, 15–17), ii) the composition of the cryovolcanic plume of Enceladus measured by the Cassini spacecraft (18, 19), and iii) remote sensing observations of Europa's surface (20–23). However, based on comparisons with hydrate phases characterized in spectral databases, no NaCl-bearing solid species have been identified in infrared reflectance spectroscopic observations of Europa and Ganymede.

Author contributions: B.J. designed research; B.J., A.P., I.E.C., S.P., T.B.B., S.D.V., S.C., V.B.P., D.H., and J.O. performed research; B.J., A.P., I.E.C., S.P., T.B.B., J.M.B., S.C., V.B.P., K.G., G.G., D.C., and M.H. contributed new reagents/analytic tools; B.J., A.P., I.E.C., and T.B.B. analyzed data; and B.J. wrote the paper with feedback from all authors.

The authors declare no competing interest.

This article is a PNAS Direct Submission.

[1]To whom correspondence may be addressed. Email: bjournau@uw.edu.

This article contains supporting information online at https://www.pnas.org/lookup/suppl/doi:10.1073/pnas.2217125120/-/DCSupplemental.

Published February 21, 2023.

Instead, the presence of chlorinated hydrate species with large hydration numbers (e.g. Mg-bearing chloride, chlorate, and perchlorate) was suggested (24, 25). The nondetection of a NaCl containing phase on the surface of the icy worlds remains an unresolved mystery in modern planetary sciences.

Here, we report the characterization three hydrates from in situ experiments in the H_2O–NaCl systems at high pressures (up to 2,500 MPa) and low temperatures (down to 150 K) in a cryogenically cooled diamond anvil cell (DAC), using single-crystal X-ray diffraction (SCXRD), and Raman spectroscopy. Details on the experimental methods are provided in the material and method section, and the *SI Appendix*, Text S1. The measurements cover the entire range of conditions expected in the hydrospheres and icy crusts of ocean worlds in the Solar System (6). Finally, we review thermodynamic constraints allowing for a revised H_2O–NaCl phase diagram and discuss the planetary implication of such a finding.

Results

We identified three hydrate phases in the H_2O–NaCl systems in the 150 to 300 K temperature range and up to 2,500 MPa (25 kbar). We refined the crystal structures of two previously unreported sodium chloride hydrates at high pressures: the disodium chloride decaheptahydrate, $2NaCl{\cdot}17H_2O$ (SC8.5), and the sodium chloride decatriahydrate, $NaCl{\cdot}13H_2O$ (SC13). We also report the symmetry and lattice parameters of a third phase, though a structure solution for this phase could not be obtained due to the difficulty in centering the very thin needle-like crystals resulting in insufficient data quality. All three phases were identified several times during three experimental runs at the European Synchrotron Radiation Facility (ESRF) (beamline ID15B) and Deutsches Elektronen-Synchrotron (DESY) Petra III (beamline P02.2) synchrotron facilities. The followed thermodynamic paths and details of the structure refinements are provided in *SI Appendix*, Text S1 and S2, respectively. The crystallographic information files (CIFs) for the reported structures are deposited in *SI Appendix* as well as at the inorganic crystal structure database (ICSD) under deposition numbers CSD 2203504–2203505.

Crystal Structures. Disodium chloride decaheptahydrate, $2NaCl{\cdot}17H_2O$, (SC8.5), or $[Na(H_2O)_6]Cl{\cdot}2.5(H_2O)$ in the International Union of Pure and Applied Chemistry (IUPAC) nomenclature, was formed by cooling a 4 mol/kg NaCl aqueous solution to 180 K near 300 MPa. It has a monoclinic unit cell (*C2/c* space group) with unit-cell lattice parameters a = 15.0132(4) Å, b = 6.08030(10) Å, c = 21.9946(18) Å and β = 103.086(5)^0, corresponding to a volume of V = 1,955.63(18) Å^3 at 450 MPa and 243 K. The structure is illustrated in Fig. 1*A*, crystal habits are shown in Fig. 1*B* and cystallographic data reported in supplementary materials (CIF file, and *SI Appendix*, Table S2). Only hydrogen positions that could be identified in the Fourier difference maps (~23.5%) were included in the refinement. $2NaCl{\cdot}17H_2O$ is composed of layers of fully dissociated sodium and chlorine ions organized along the (001) plane. The sodium layer has two rows of $[Na(H_2O)_6]^+$ octahedra in a zigzag arrangement, with neutral water molecules located around these octahedra, while the chlorine layer is solely composed of Cl^- ions. The closest separations between the $[Na(H_2O)_6]^+$ octahedra are found at 5.6 Å between the top and bottom octahedra in the double layer. The closest Cl^- ion separation within its layer is at 4.2 to 4.6 Å. The refined hydrogens are pointing away from the Na^+ ions and are oriented toward the Cl^- ions and neighboring water molecules (*SI Appendix*, Fig. S2). This configuration is similar to the clustered structures in aqueous NaCl (26). Within the octahedra, the Na^+–O distances are between 2.36 and 2.47 Å. Chlorine ions are in a distorted sevenfold coordination with H_2O molecules, with the Cl–O distances ranging from 3.10 to 3.29 Å. The average O–O distance is 2.83 Å between hydrogen-bonded water molecules, with a OH–O bond of approximately 2.0 Å. In halite and hydrohalite, Na^+ and Cl^- ions have ionically bonded separations of 2.72 Å and 2.80 Å, respectively (10). The shortest Na–Cl distance in SC8.5 is 4.26 Å, confirming that the two atoms are fully dissociated. At the pressure and temperature of the X-ray analysis, the $2NaCl{\cdot}17H_2O$ density is 1,437 kg m^{-3}, denser than high-pressure ice polymorph II, which has a density of 1,201 kg m^{-3} at the same conditions (27).

The second hydrate is sodium chloride decatriahydrate, $NaCl{\cdot}13H_2O$ (SC13), or $[Na(H_2O)_6]Cl{\cdot}7(H_2O)$ in IUPAC nomenclature. It was formed by cooling a 4 mol/kg NaCl aqueous solution to 270 K near 1,500 MPa or by warming an ice VI + SC2 mixture above 290 K at 1,230 MPa (*SI Appendix*, Text S1.3). Its structure is illustrated in Fig. 1*C* and cystallographic data reported in supplementary materials (CIF file, and *SI Appendix*, Table S2). It also has a monoclinic unit cell (*I2/m* space group) with lattice parameters a = 10.9150(3) Å, b = 11.8900(10) Å, c = 11.2752(5) Å and β= 118.307(8)^0, with a volume of V = 1,288.3(3) Å^3 (1,509 kg m^{-3}) at 1,500 MPa and 295 K. Only hydrogen positions that could be identified in the Fourier difference maps (~42%) were included in the refinement. $NaCl{\cdot}13H_2O$ is composed of $Na^+(6H_2O)$ octahedra organized in columns along the <100> direction, with interstitial Cl^- ions (*SI Appendix*, Fig. S4). Compared with the SC8.5 structure, both ions are found in single layers, and the water molecules are located in both the sodium and chlorine layers (Fig. 1*C*). Closest pairwise Cl–Cl separations are at 3.65 Å, with the next pairwise Cl–Cl distance at 8.0 Å due to the presence of the water molecules in between. The $[Na(H_2O)_6]^+$ octahedra are equally separated at 5.46 Å. Na^+–O distances in the octahedron are between 2.32 and 2.40 Å. Na^+ and Cl^- ions are, again, fully dissociated with the closest distance being 4.2 Å. At these conditions, the $NaCl{\cdot}13H_2O$ density is 1,509 kg m^{-3}, roughly 8.5% denser than ice VI, the stable water polymorph at these conditions, with a density of 1,390 kg m^{-3} (27).

A third phase was observed in the pressure and temperature range of stability of ice V. It was formed through cooling a 4 mol/kg NaCl aqueous solution near 500 MPa and appeared with a needle-like habit (Fig. 1*E*). Several attempts to grow larger crystals were not successful, and the quality of the X-ray diffraction patterns was inadequate to refine the structure. The unit-cell lattice parameters were determined to be in the *C2/c* space group with a = 6.78(1) Å, b = 45.14(2) Å, c = 9.23(1) Å, β = 109.8(1)^0, V = 2657.1(1) Å^3, at 500 MPa and 238 K. Under near-liquidus conditions (Fig. 1*F*), the crystals sank to the bottom of the DAC, suggesting that they are denser than the coexisting fluid and, thus, contain NaCl in their structure.

In our experiments, ice II was identified along with disodium chloride decaheptahydrate (SC8.5) and the NaCl aqueous solution at 450 MPa and 243 K (Fig. 1*B*). This finding may not represent a reliable measurement of the triple point because a chemical gradient in the fluid may arise due to the high viscosity of the brine at low temperatures. The ice II crystals float in the concentrated NaCl brine, as also observed for ice VI at higher pressures in solutions with concentrations above 2.5 mol/kg (28). This is, to our knowledge, the only reported in situ observation of a well-developed ice II crystal habit, and observation of ice II coexisting with aqueous fluid, previously only predicted for the H_2O-NH_4 system (29). As shown in Fig. 1*B*, ice II formed near equant rhombohedra, consistent with its *R3* space group.

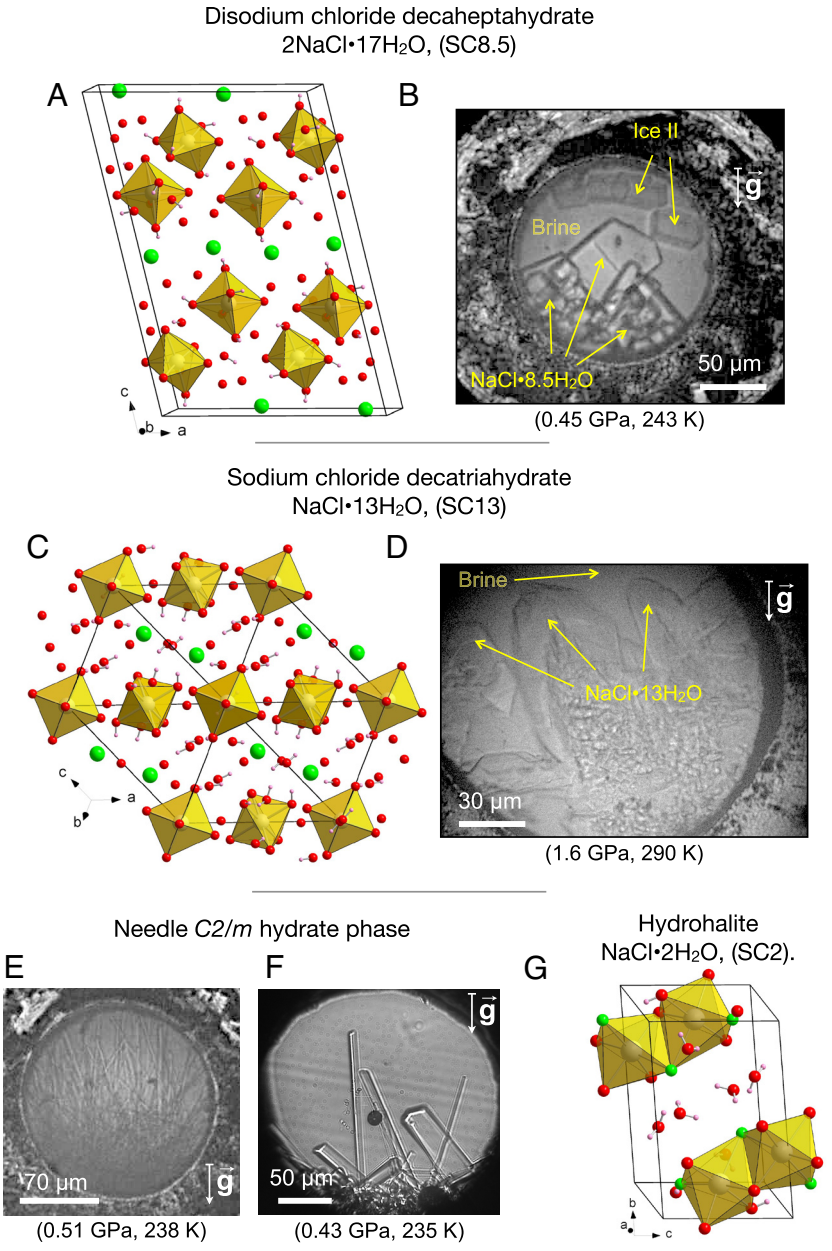

Fig. 1. Crystal structures and microphotographs of NaCl hydrates. (*A*) Refined crystal structure of disodium chloride decaheptahydrate $2NaCl{\cdot}17H_2O$ (SC8.5). $[Na(H_2O)_6]^+$ units are represented by yellow colored octahedra; the spheres represent locations of Na^+ (yellow), Cl^- (green), O (red), and solved hydrogen positions in pink. (*B*) Microphotograph of SC8.5 in equilibrium with ice II and the brine taken at the ID15B beamline, ESRF, France. The gravity vector direction is indicated. (*C*) Crystal structure of sodium chloride decatriahydrate $NaCl{\cdot}13H_2O$ (SC13). (*D*) Microphotograph of SC13 in equilibrium with brine taken at the P02.2 beamline, DESY PETRA III, Germany. (*E*) Microphotograph of the *C2/c* needle hydrate phase taken at the ID15B beamline and (*F*) at the APS GSECAR beamline, USA. (*G*) Crystal structure of hydrohalite $NaCl{\cdot}2H_2O$ (SC2) (10).

Raman Spectra. Raman spectra (Fig. 2) for disodium chloride decaheptahydrate $2NaCl{\cdot}17H_2O$ (SC8.5), the *C2/c* needle hydrate, and hydrohalite (only stretching modes) were collected using the offline DAC optimized confocal Raman system at the GSECARS beamline at the Advanced Photon Source (APS) (details in the *Materials and Methods*). Phases were formed by following the same thermodynamic path, at similar liquidus conditions and checking for similar crystallographic habits as with previous SCXRD experiments. Hydrohalite displays typical 3,420 and 3,542 cm^{-1} peaks in the stretching region. The SC8.5 hydrate displays three distinctive peaks at 3,404, 3,450, and 3,511 cm^{-1} in the stretching region. These peaks are almost identical to the spectra collected by ref. 13 on an unidentified columnar phase taken at higher pressures, suggesting it is the same phase. We also observed a strong dependance of the stretching peaks' relative intensities with the crystal orientation, as shown in Fig. 2 with the two different spectra taken on two different crystallites (bottom spectra mixed with the signal of ice V stretching modes). It also appears that the last peak around 3,511 cm^{-1} can decompose into a 3,509 + 3,524 cm^{-1} doublet when a different crystal orientation is used. The *C2/c* needle hydrate stretching spectrum has a broader peak center around 3,460 cm^{-1} and another smaller contribution close to 3,499 cm^{-1}. The lattice mode regions of SC8.5 and of the needle hydrates have a complex collection of different Raman peaks, as shown in Fig. 2.

Thermodynamic Stability. The solid phase with the highest temperature liquidus at a given pressure is the most stable since superheating in the liquid regime is negligible. In contrast, solid–solid phase transitions show significant hysteresis or even nonreversibility depending on the thermodynamic paths (27)

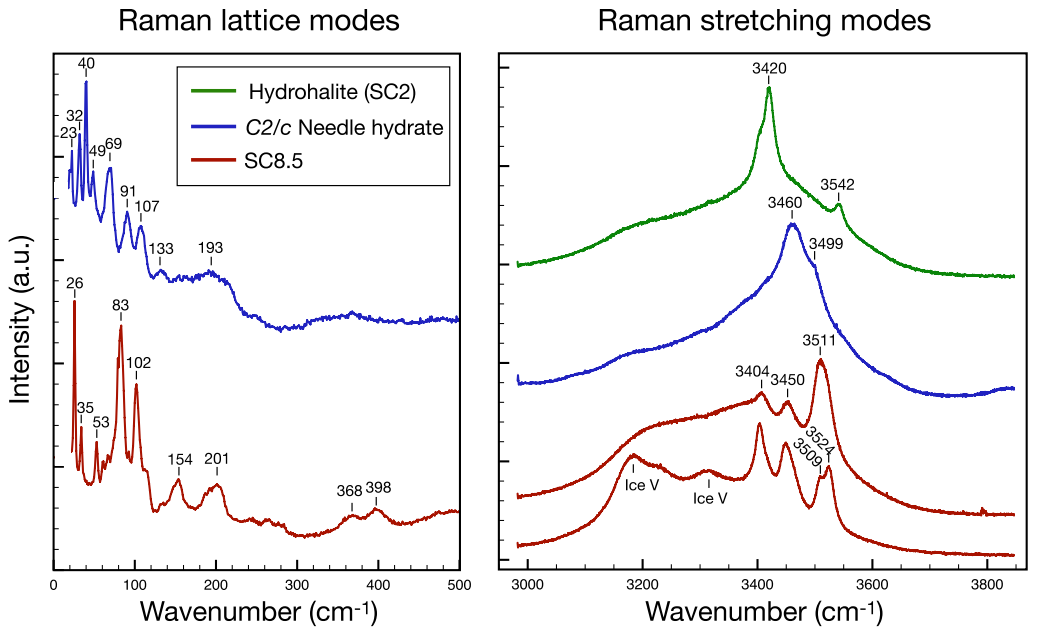

Fig. 2. Raman Spectra of NaCl hydrates. Disodium chloride decaheptahydrate $2NaCl{\cdot}17H_2O$ (SC8.5) measured at 0.42 GPa and 245 K, *C2/c* needle hydrate at 0.43 GPa and 235 K and hydrohalite (SC2, only stretching) at 1.05 GPa and 275 K. Two stretching modes spectra for SC8.5 (with possible ice V contributing peaks) are reported to illustrate the effect of crystal orientation.

as a result of the metastability of phases. Hereafter, we used liquidus measurements (filled symbols in Fig. 3) to determine phase boundaries and which solid phases are thermodynamically stable. Other points reported in Fig. 3 show identification of phases during exploration over the range of conditions.

The SC8.5 liquidus (blue filled circles) at 4 mol/kg was observed around 10 K above the estimated melting point of ice V and ice VI in equilibria with 4 mol/kg $NaCl_{(aq)}$ (red and blue dotted lines, respectively) (28) up to 700 MPa. Thus, SC8.5 is a stable solid phase in the H_2O–NaCl system at pressures between 300 and 700 MPa. At those pressures, it therefore becomes the stable hydrate at the eutectic with the ice (II, III, V, or VI) and the liquid.

SC13 has liquidus points (purple filled square in Fig. 3) at lower temperatures than the measured liquidus of ice VI in 4 mol/kg $NaCl_{(aq)}$ (blue dotted curve) (28). We also observed SC13 melting before ice VI upon warming, showing it is not the stable phase at the liquidus at 4 mol/kg. Nevertheless, our results are compatible with SC13 being a stable phase at the liquidus at a higher concentration, above the high-pressure ice VI-SC13-liquid eutectic. Similarly, the *C2/c* needle phase has been observed (turquoise diamonds in Fig. 3) very close under the estimated melting curve of ice V at 4 mol/kg (red dotted curve). From these data, we cannot conclude on its stability/metastability. These findings need to be further investigated in future studies for both hydrates.

Below liquidus conditions, SC2, SC8.5, and SC13 can all be compressed to 2,000 MPa along an isothermal path without destabilization. However, we observed several times that SC8.5 destabilizes upon warming above 273 K and above 1,000 MPa into ice VI + SC2, then to ice VI + SC13 (*SI Appendix*, Text S1), suggesting that SC8.5 is only stable below this temperature. Furthermore, when pressurized beyond the ice VI – ice VII solid–solid transition around 2,200 MPa, an assemblage of ice VI and SC2 transformed into salty ice VII and crystalline NaCl (see *SI Appendix*, Text S1 for details).

To test the stability of SC8.5 under icy moon surface conditions, we performed a quenching experiment shown with an orange arrow in Fig. 3. We cooled the SC8.5 phase down to 150 K at about 250 MPa (1 K/min) and then gradually isothermally decompressed it over 1 h down to the minimum achievable with the experimental setup within the uncertainty of the ruby pressure measurement (±30 MPa), potentially opening the cell and exposing the sample to the cryostat pressure ($<10^{-5}$ bar). There, SC8.5 was found together with ice I h, suggesting that SC8.5 is stable or metastable at near-vacuum conditions, or at least down to <30 MPa. Upon subsequent heating (1 K/min), the ice I h + SC8.5 assemblage transformed into ice I h + SC2 between 210 and 240 K (black interval on Fig. 3). The SC8.5 liquidus was extended to 1 bar (cyan line in Fig. 3, details in *SI Appendix*, Text S3 and Fig. S6) based on our liquidus measurements at 4 mol/kg (filled blue circles) and supported by liquidus measurements at 5.7 mol/kg (columnar phase with the same Raman spectra) (13). The estimated metastable 4 mol/kg liquidus of SC8.5 at 1 bar is around 230 K (blue star in Fig. 3), in the same range where we observed the SC8.5 → SC2 + ice I-h transition.

Discussion

Hydrate Structure and Hyperhydration. The finding of three hydrate phases of NaCl opens a different perspective in physical chemistry. These phases stand out as the only 8.5 and 13 hydrates, providing evidence for a greater diversity of hydrates and hydrogen-bonded crystal structures than previously recognized. The discovery of stable NaCl hydrates containing many waters of hydration (stoichiometric number of H_2O molecules per salt ions pair) is surprising. Other alkali halides have a small number of waters of hydration, less than five in most cases as for example NaF ($NaF{\cdot}H_2O$), NaBr ($NaBr{\cdot}H_2O$, $NaBr{\cdot}2H_2O$), NaI ($NaI{\cdot}H_2O$), LiCl ($LiCl{\cdot}2H_2O$, $LiCl{\cdot}3H_2O$, $LiCl{\cdot}5H_2O$), and KCl ($KCl{\cdot}H_2O$, $KCl{\cdot}2H_2O$) (30). Furthermore, the crystal structures of diatomic alkali halide hydrates typically consist of ionically bounded pairs, as in hydrohalite (SC2, in Fig. 1*G*). In the case of SC8.5 and SC13, both crystalline phases have fully dissociated ions, which will be hereafter referred as "hyperhydrated" structures. This effect is common for larger molecular salts that often form hydrates with many waters of hydration. For example, the H_2O–$MgSO_4$ system has 11 reported hydrate phases with up to 11 water molecules per $MgSO_4$ (31–34). Other common inorganic

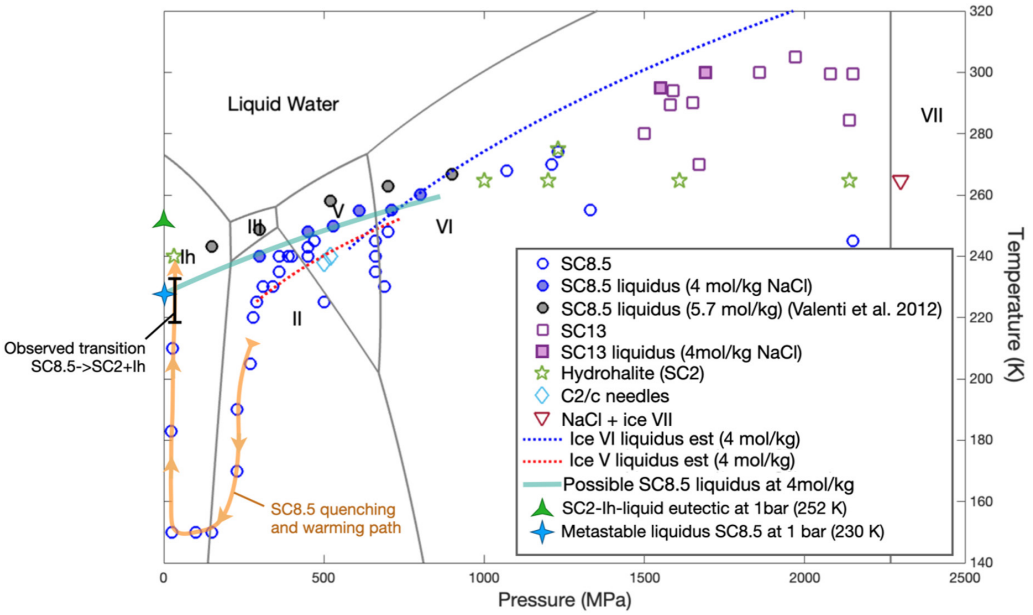

Fig. 3. Experimental data pressure and temperature coordinates for the different phases identified with X-ray diffraction. The pure water phase diagram computed with SeaFreeze is shown as gray lines for comparison (27). Estimation of ice V and ice VI 4 mol/kg liquidus is based on the ice VI measured melting point depression that was measured to be at least 25 K (28).

molecular salt hydrates behave in the same manner, for example Na_2SO_4 (7 and 10 H_2O), $NaPO_4$ (0.5, 1, 2, 6, 7, 8, and 12 H_2O) and $MgCl_2$ (1, 2, 4, 6, and 8 H_2O) (35–38). Higher hydration number results in structures where the ionic compounds are fully dissociated, with the cation usually in a $X^{n+}(H_2O)_6$ octahedral configuration (30, 34, 36, 38, 39), and even $X^{n+}(H_2O)_8$ antiprism configurations for $CaBr_2$ and CaI hydrates (37). That alkali halide hydrates do not tend to form hyperhydrated structures at room conditions may be due to the high ionic bonding energy of simple salt compounds compared with larger molecular salts. In the case of most alkali halides under standard conditions, electrostatic interactions between the ions and a water-molecule-based lattice are not strong enough for ionic dissociation. Our results suggest that higher pressure aids formation of hyperhydrated species for simple inorganic salts by increasing electrostatic interactions between H_2O molecules and the salt species. This effect would ease ionic dissociation and enable formation of hyperhydrated $X^{n+}(H_2O)_6$ octahedral configurations as seen in SC8.5 and SC13 for NaCl (Fig. 1 *A* and *C*). We hypothesize that additional hyperhydrated phases will be found at low temperatures and pressures below 2,000 MPa. This study should motivate future experimental and computational efforts to explore the diversity of hydrated species and hydrogen-bound crystallographic structures.

Updates to the H_2O–NaCl Phase Diagram. The finding of stable hydrates in the H_2O–NaCl binary system implies modifications to its phase diagram, which has not changed significantly since the description of hydrohalite in 1847 (40). Our experimental observations allow us to study the stability of SC8.5 at ambient pressure. Using the fits of the liquidus surface of SC8.5 and SC2 (*SI Appendix*, Text S3 and Fig. S6), we can project the metastable liquidus lines onto the 1 atmosphere H_2O–NaCl phase diagram on Fig. 4. The metastable liquidus of SC8.5 can be seen as a blue dashed line, and the SC2 liquidus metastable extension as a gray dashed line. The two lines intersect around 4.5 mol/kg and 235 K at the metastable liquid–SC2–SC8.5 triple point (purple point on Fig. 4), which is a metastable peritectic. Below this point, the SC8.5 liquidus (dashed blue line on Fig. 4) is at a higher temperature than the SC2 liquidus (dashed gray line on Fig. 4), meaning that SC8.5 has a lower Gibbs free energy than SC2 and therefore becomes the thermodynamically preferred phase below 235 K when in equilibrium with metastable brine. Combined with the experimental measurement of the SC8.5 → SC2 + ice I-h transition between 210 and 240 K, this finding suggests that the SC8.5–SC2–ice Ih triple phase line should be in the vicinity of these temperatures. Therefore, we estimate the position of the SC8.5–SC2–ice Ih equilibrium line around 235 K (±10 K). The updated phase diagram (Fig. 4) displays two coexistence stability fields below 235 K: Ih+SC8.5 up to 26.6 wt% NaCl (stoichiometric composition of SC8.5), and SC8.5+SC2 up to the transition SC2 + NaCl at 61.9 wt%.

That SC8.5 was previously unknown could result from the lack of observations below 235 K using methods that could characterize structures. Additionally, the reaction timescale for SC2 + ice Ih → SC8.5 might be significantly slower than the duration of experiments using cryogenic X-ray diffraction of, at most, a few days. It is nonetheless possible that SC8.5 might exist as a mineral species in cold and briny lakes of the Antarctic dry valleys where temperatures can be as low as 223 K during the winter season (41). Previous Raman measurements on Don Juan Pond salt hydrates were made from samples stored and examined under conditions (42) above the SC2 + ice Ih → SC8.5 transition. The Raman spectra for SC8.5 provided in Fig. 2 will be of great help in future investigations aimed at mapping the presence of SC8.5 at low temperatures and 1 atmosphere.

At elevated pressures (300 to 700 MPa), we point out that SC8.5 is likely a stable NaCl hydrate at the eutectic conditions, and SC13 stability remains to be verified. A schematic of the high-pressure phase diagram of H_2O–NaCl is given in *SI Appendix* at 400 and 1,500 MPa (*SI Appendix*, Fig. S7). Our results also suggest the destabilization of hydrates beyond the ice VI–ice VII phase transition at 2,200 MPa, which would imply that no NaCl hydrates are stable within the ice VII stability field in the H_2O–NaCl system, apart from ice VII itself (43, 44). This may be due to the fact that ice VII is able to incorporate up to several molar of salts (43–45).

Planetary Science Implications. Because of the large range of P–T conditions expected inside icy ocean worlds (6, 46), the identified NaCl hyperhydrates will form in different layers of their

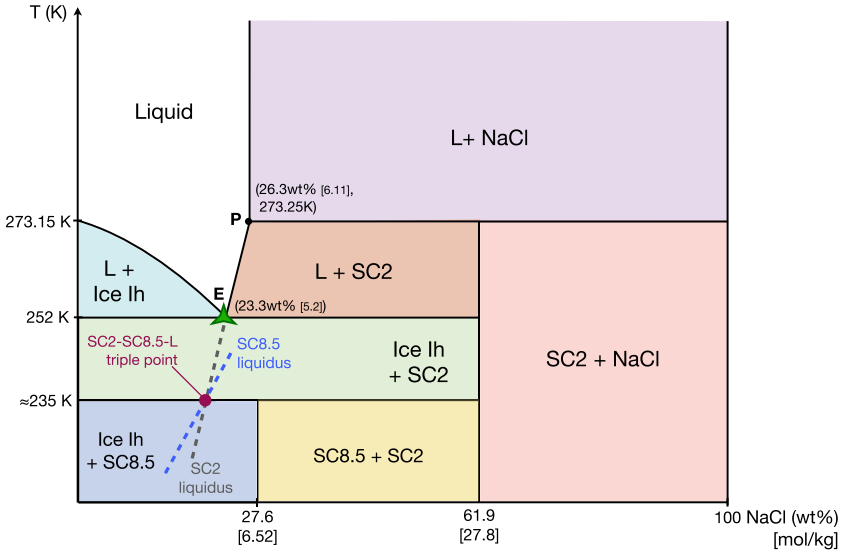

Fig. 4. Proposed update to the H_2O–NaCl phase diagram at 1 bar. SC8.5 becomes a stable NaCl hydrate below around 235 K. The green triangle (E) is the SC2–Ih–liquid eutectic, and P is the NaCl–SC2–liquid peritectic point.

hydrosphere, (Fig. 5). In the outer crust of ice-covered moons, the formation of SC8.5 must take place in the upper few kilometers of the conductive ice shell at temperatures below 235 K (46) (Fig. 5). Deeper convective parts (46) are likely at temperatures above the stability range of SC8.5 at low pressures. The slow vertical exchange expected within the brittle layer associated with tectonic processes (14, 47) could compensate for slow kinetics of the SC2 + ice Ih → SC8.5 reaction. Our results also suggest that SC8.5 remained stable down to the ice-surface to near-surface pressures in ocean worlds, within measurement uncertainty. Long-term stability at the surface remains to be studied, especially under the intense radiation condition occurring at the surface of Europa (20). The presence of SC8.5 in surface materials could be used to identify and characterize regions of extrusion of oceanic material frozen at depth. Such an indicator of vertical exchange would aid in the search for biosignatures by upcoming missions such as ESA's JUICE, NASA's Europa Clipper and DragonFly (7–9), and future landers (48, 49).

Deeper within large icy worlds like Ganymede, Titan, and Callisto (6), SC13 and SC8.5 are stable at the eutectic within the high-pressure ice mantle (Fig. 5). If NaCl is the major solute in a given large ocean world, they will be the major nonice species in the high-pressure ice shell. The deep high-pressure ice mantles in large icy worlds likely have complex melting/freezing processes at the ice-ocean and ice-rocky core boundaries (50) (mush layer on Fig. 5). At the top of the high-pressure ice mantle of these large

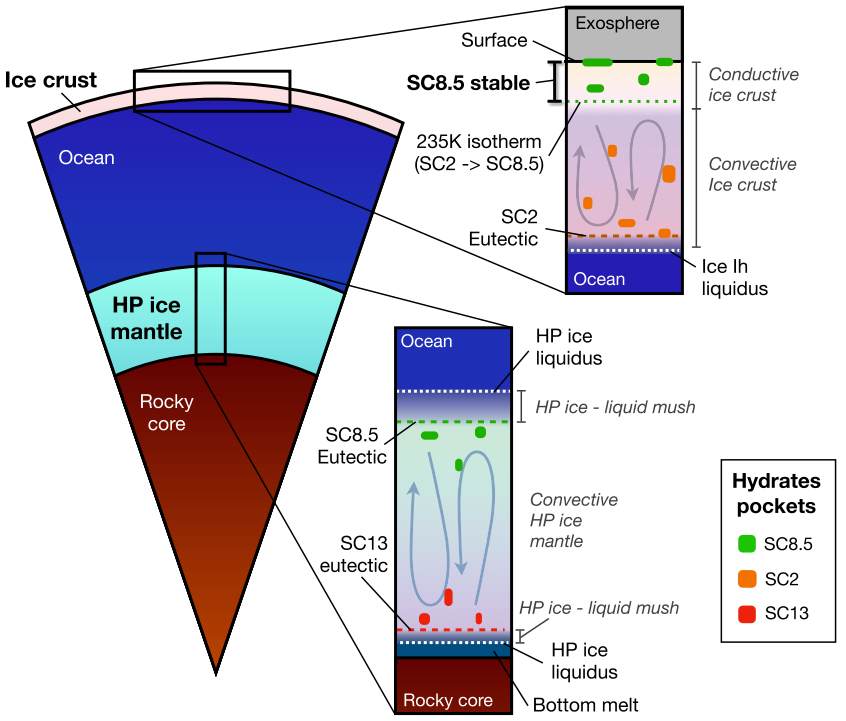

Fig. 5. Schematic structure of a large icy moon on the left with respective stability region (*Right*) of each hydrates depending on thermodynamic conditions. The *Upper Right* panel on the upper icy crust also applies to smaller icy ocean worlds like Europa and Enceladus.

moons, the conditions are expected to be below 275 K (6), making SC8.5 the most probable hydrate to form. At the bottom of the high-pressure ice mantle, we expect temperatures in excess of 280 K, making SC13 the most likely hydrate at the base. In such context, the SC8.5 <–> SC13 transition would happen at the 275 K isotherm within the convective high-pressure ice shell. Depending on the hydrate, the ice-hydrate mixture will have change in properties (e.g., density, heat capacity, and rheology) that will directly affect the geodynamic and chemical vertical transport of important solutes and nutrients through the high-pressure shell (50, 51).

Finally, the absence of an identified NaCl bearing species on icy world surfaces represents an important quandary in planetary science. Geochemical modeling (5, 16), in situ mass spectroscopy of icy grains in Enceladus plumes (18), and optical/UV cues (21–23) all point toward NaCl being widespread at the surface of Europa and Ganymede. However, near-infrared spectral signatures of hydrated species on their surface cannot be explained by hydrohalite (SC2) (52). In the absence of adequate NaCl hydrate phases in spectral databases, several studies have tried to fit the remote sensing spectra with various other hydrates. They have found that species with high water of hydration and often hyperhydrated structures, including sulfates, or the chlorinated species—chlorate (ClO_3^-) or perchlorate (ClO_4^-) hydrates (24, 53)—increase the depth and width of water bands overtones, required to fit the near infrared surface spectra. Our thermodynamic data support the existence SC8.5 as a stable NaCl-bearing hyperhydrated phase on icy surfaces of the outer solar system bodies such as Europa, Titan, Ganymede, Callisto, Enceladus, or Ceres, where surface temperatures are well under 235 K. Its infrared spectra remain to be determined in future studies, but its hyperhydrated structure could solve the long-standing mystery of the unidentified hydrate phase at the surface of Europa and Ganymede (24, 25, 52).

Materials and Methods

High-Pressure X-ray Diffraction Experiments. Four series of in situ X-ray diffraction experiments have been performed. Experiment 1 and experiment 4 were performed at the ESRF (Grenoble, France) ID15B beamline in two separate beamtimes. Experiments 2 and 3 refer to data collected with two different loadings during the same beamtime at the P02.2 beamline of Deutsches Elektronen Synchrotron (DESY, Hamburg, Germany). Membrane-driven Le Toullec-type and Mao-type diamond anvil cells (DACs) with culet diameter of 700 μm were used for pressure generation. The sample chambers with the approximate diameter of 500 μm were obtained by drilling stainless steel gaskets preindented to 80 μm. A mixture of ultrapure MiliQ™ water with NaCl (4 mol/kg solution) was loaded in the sample chambers along with a ruby sphere as a pressure calibrant. In addition, an external ruby was placed on the back of the diamond anvil to correct for the temperature dependency of the ruby fluorescence, providing pressure estimation error of 30 MPa (27). Temperature was regulated using in-house He-cryostats available at the ID15B beamline of the ESRF (Grenoble, France) and at the P02.2 beamline of Deutsches Elektronen Synchrotron (DESY, Hamburg, Germany). Single-crystal X-ray diffraction experiments were performed using monochromatic X-rays with wavelengths of 0.41505 Å and 0.2897 Å at ID15B and P02.2 beamlines, respectively. The X-ray beam was focused to ~10 × 10 μm^2 and ~d8 (h) × 3 (v) μm^2 by beryllium compound refractive lenses at the beamlines ID15B and P02.2, respectively. Diffraction images were collected using a MAR555 flat panel detector (Experiment 1) and EIGER2 X CdTe 9M detector (Experiment 4) at the ESRF and using a Perkin Elmer detector at DESY (Experiments 2 and 3). The detector-sample distance was calibrated with a Si or CeO_2 standard at the ESRF and DESY, respectively, using the procedure implemented in the program Dioptas (54). Data collection on single crystals was performed as a series of ω scans in a range ±28° (Experiments 2 and 3) or ±30° (Experiments 1 and 4) with exposures taken every 0.5° for up to 2 s. The unit-cell lattice parameters and the integrated intensities of the Bragg reflections were obtained from the measured images using the program CrysAlisPro™. Details on the crystal structure solution and refinements are reported in *SI Appendix*, Text S2.

Raman Spectroscopy. Raman spectra were collected on the DAC optimized confocal Raman system at GSECARS (55) at Advanced Photon Source, equipped with ultralow frequency (<10 cm^{-1}) Raman edge filters and a deep-depleted back illuminated charge-coupled device (CCD) detector (PIXIS100 from Princenton Instruments™). We used the narrow line excitation wavelength at 532 nm and a 500 nm/1,200 cm^{-1} grating. The DAC was placed in the in-house developed N cryostat operated under vacuum to typically ~1×10^{-6} bar. We used a mBX90 mini diamond anvil cell (56) with culet diameter of 700 μm with a 500-μm pressure chamber drilled in a stainless steel preindented at 80 μm. A mixture of ultrapure MiliQ™ water with NaCl (4 mol/kg solution) was loaded in the sample chamber along with a ruby sphere as a pressure calibrant.

Data, Materials, and Software Availability. CIF files are available in supplementary materials and have been deposited in Inorganic Crystal Structure Database (CSD 2203504–2203505). All study data are included in the article and/or *SI Appendix*.

ACKNOWLEDGMENTS. We thank Evan Abramson, Matthew Powell-Palm, and Vincent Chevrier for the insightful discussions about the thermodynamics of aqueous systems that helped with this work. We acknowledge the financial support provided by the NASA Postdoctoral Program fellowship awarded to B.J., by the NASA Solar System Workings Grant 80NSSC17K0775, by the Icy Worlds and the Titan and Beyond nodes of NASA Astrobiology Institute (08-NAI5-0021 and 17-NAI82-17). Synchrotron radiation experiments were conducted under beamtime granted to B.J. at the ID15B beamline (proposal number ES807 and HC4440) at the ESRF, Grenoble, France. We acknowledge DESY (Hamburg, Germany), a member of the Helmholtz Association, for the provision of experimental facilities. Parts of this research were carried out at P02.2 beamline of Petra III synchrotron. Beamtime was allocated for proposal 11007190. J.O. financial support was provided by the Department of Earth and Space Science of the University of Washington, Seattle, USA. Use of the GSECARS Raman Lab System was supported by the NSF MRI Proposal (EAR-1531583). A part of the research was carried out at the Jet Propulsion Laboratory, California Institute of Technology, under a contract with the NASA (80NM0018D0004).

Author affiliations: [a]Department of Earth and Space Sciences, University of Washington, Seattle, WA 98195; [b]Deutsches Elektronen-Synchrotron, D-22607 Hamburg, Germany; [c]European Synchrotron Radiation Facility, 38000 Grenoble, France; [d]Center for X-ray Analytics, Empa – Swiss Federal Laboratories for Materials Science and Technology, 8600 Dübendorf, Switzerland; [e]Institute of Geochemistry and Petrology, ETH Zürich, 8092 Zürich, Switzerland; [f]Bayerisches Geoinstitut, University of Bayreuth, 95440 Bayreuth, Germany; [g]Jet Propulsion Laboratory, California Institute of Technology, Pasadena, CA 91109; and [h]Center for Advanced Radiations Sources, University of Chicago, Chicago, IL 60637

1. M. Elimelech, W. A. Phillip, The future of seawater desalination: Energy, technology, and the environment. *Science* **333**, 712–717 (2011).
2. C. E. Manning, The chemistry of subduction-zone fluids. *Earth Planet. Sci. Lett.* **223**, 1–16 (2004).
3. A. Polidori *et al.*, Structure and dynamics of aqueous NaCl solutions at high temperatures and pressures. *J. Chem. Phys.* **155**, 194506 (2021).
4. W. Wei, J. Xu, W. Chen, L. Mi, J. Zhang, A review of sodium chloride-based electrolytes and materials for electrochemical energy technology. *J. Mater. Chem. A* **10**, 2637–2671 (2022).
5. F. Sohl *et al.*, Subsurface water oceans on icy satellites: Chemical composition and exchange processes. *Space Sci. Rev.* **153**, 485–510 (2010).
6. B. Journaux *et al.*, Large ocean worlds with high-pressure ices. *Space Sci. Rev.* **216**, 7 (2020).
7. O. Grasset *et al.*, JUpiter ICy moons Explorer (JUICE): An ESA mission to orbit Ganymede and to characterise the Jupiter system. *Planet. Space Sci.* **78**, 1–21 (2013).
8. C. B. Phillips, R. T. Pappalardo, Europa clipper mission concept: Exploring Jupiter's ocean moon. *Eos Trans. Am. Geophys. Union* **95**, 165–167 (2014).
9. R. D. Lorenz, E. P. Turtle, J. W. Barnes, M. G. Trainer, Dragonfly: A rotorcraft lander concept for scientific exploration at titan. *Johns Hopkins APL Tech. Dig.* **34**, 14 (2018).
10. B. Klewe, B. Pedersen, The crystal structure of sodium chloride dihydrate. *Acta Crystallogr. B* **30**, 2363–2371 (1974).
11. L. Adams, Equilibrium in binary systems under pressure. I. An experimental and thermodynamic investigation of the system, NaCl-H2O, at 25°. *J. Am. Chem. Soc.* **53**, 3769–3813 (1931).

12. S. Sawamura, N. Egoshi, Y. Setoguchi, H. Matsuo, Solubility of sodium chloride in water under high pressure. *Fluid Phase Equilibria* **254**, 158–162 (2007).
13. P. Valenti, R. J. Bodnar, C. Schmidt, Experimental determination of H2O–NaCl liquidi to 25mass% NaCl and 1.4GPa: Application to the Jovian satellite Europa. *Geochim. Cosmochim. Acta* **92**, 117–128 (2012).
14. S. D. Vance, B. Journaux, M. Hesse, G. Steinbrügge, The salty secrets of icy ocean worlds. *J. Geophys. Res. Planets* **120**, e2020JE006736 (2020).
15. M. Y. Zolotov, J. S. Kargel, "On the chemical composition of Europa's icy shell, ocean, and underlying rocks" in *Europa* (University of Arizona Press, 2009).
16. M. Y. Zolotov, Aqueous fluid composition in CI chondritic materials: Chemical equilibrium assessments in closed systems. *Icarus* **220**, 713–729 (2012).
17. M. Melwani Daswani, S. D. Vance, M. J. Mayne, C. R. Glein, A Metamorphic origin for Europa's ocean. *Geophys. Res. Lett.* **48**, e2021GL094143 (2021).
18. F. Postberg, S. Kempf, J. Schmidt, N. Brilliantov, Sodium salts in E-ring ice grains from an ocean below the surface of Enceladus. *Nature* **459**, 1098–1101 (2009).
19. F. Postberg, J. Schmidt, J. Hillier, S. Kempf, A salt-water reservoir as the source of a compositionally stratified plume on Enceladus. *Nature* **474**, 620–622 (2011).
20. M. E. Brown, K. P. Hand, Salts and radiation products at the surface of Europa. *Astron. J.* **145**, 110 (2013).
21. K. P. Hand, R. W. Carlson, Europa's surface color suggests an ocean rich with sodium chloride: Sodium chloride on Europa's surface. *Geophys. Res. Lett.* **42**, 3174–3178 (2015).
22. S. K. Trumbo, M. E. Brown, K. P. Hand, Sodium chloride on the surface of Europa. *Sci. Adv.* **5**, eaaw7123 (2019).
23. S. K. Trumbo *et al.*, A new UV spectral feature on Europa: Confirmation of NaCl in leading-hemisphere chaos terrain. *Planet. Sci. J.* **3**, 27 (2022).
24. J. Hanley, J. B. Dalton, V. F. Chevrier, C. S. Jamieson, R. S. Barrows, Reflectance spectra of hydrated chlorine salts: The effect of temperature with implications for Europa. *J. Geophys. Res. Planets* **119**, 2370–2377 (2014).
25. N. Ligier, F. Poulet, J. Carter, R. Brunetto, F. Gourgeot, VLT/SINFONI observations of Europa: New insights into the surface composition. *Astron. J.* **151**, 163 (2016).
26. M. K. Ghosh, S. Re, M. Feig, Y. Sugita, C. H. Choi, Interionic hydration structures of NaCl in aqueous solution: A combined study of quantum mechanical cluster calculations and QM/EFP-MD simulations. *J. Phys. Chem. B* **117**, 289–295 (2013).
27. B. Journaux *et al.*, Holistic approach for studying planetary hydrospheres: Gibbs representation of ices thermodynamics, elasticity, and the water phase diagram to 2,300 MPa. *J. Geophys. Res. Planets* **125**, e2019JE006176 (2020).
28. B. Journaux, I. Daniel, R. Caracas, G. Montagnac, H. Cardon, Influence of NaCl on ice VI and ice VII melting curves up to 6GPa, implications for large icy moons. *Icarus* **226**, 355–363 (2013).
29. M. Choukroun, O. Grasset, Thermodynamic data and modeling of the water and ammonia-water phase diagrams up to 2.2 GPa for planetary geophysics. *J. Chem. Phys.* **133**, 144502–144502–13 (2010).
30. J. Sohr, H. Schmidt, W. Voigt, Higher hydrates of lithium chloride, lithium bromide and lithium iodide. *Acta Crystallogr. Sect. C Struct. Chem.* **74**, 194–202 (2018).
31. D. L. Hogenboom, J. S. Kargel, J. P. Ganasan, L. Lee, Magnesium sulfate-water to 400 MPa using a novel piezometer: Densities, phase equilibria, and planetological implications. *Icarus* **115**, 258–277 (1995).
32. R. Nakamura, E. Ohtani, The high-pressure phase relation of the $MgSO_4$–H_2O system and its implication for the internal structure of Ganymede. *Icarus* **211**, 648–654 (2011).
33. E. L. Gromnitskaya *et al.*, The high-pressure phase diagram of synthetic epsomite ($MgSO_4{\cdot}7H_2O$ and $MgSO_4{\cdot}7D_2O$) from ultrasonic and neutron powder diffraction measurements. *Phys. Chem. Miner.* **40**, 271–285 (2013).
34. A. D. Fortes, K. S. Knight, I. G. Wood, Structure, thermal expansion and incompressibility of $MgSO_4{\cdot}9H_2O$, its relationship to meridianiite ($MgSO_4{\cdot}11H_2O$) and possible natural occurrences. *Acta Crystallogr. Sect. B Struct. Sci. Cryst. Eng. Mater.* **73**, 47–64 (2017).
35. S. Kamburov, H. Schmidt, W. Voigt, C. Balarew, Similarities and peculiarities between the crystal structures of the hydrates of sodium sulfate and selenate. *Acta Crystallogr. Sect. B Struct. Sci. Cryst. Eng. Mater.* **70**, 714–722 (2014).
36. E. Hennings, H. Schmidt, W. Voigt, Crystal structures of hydrates of simple inorganic salts. I. Water-rich magnesium halide hydrates $MgCl_2{\cdot}8H_2O$, $MgCl_2{\cdot}12H_2O$, MgBr 2·$6H_2O$, $MgBr_2{\cdot}9H_2O$, $MgI_2{\cdot}8H_2O$ and $MgI_2{\cdot}9H_2O$. *Acta Crystallogr. C* **69**, 1292–1300 (2013).
37. E. Hennings, H. Schmidt, W. Voigt, Crystal structures of hydrates of simple inorganic salts. II. Water-rich calcium bromide and iodide hydrates: $CaBr_2{\cdot}9H_2O$, $CaI_2{\cdot}8H_2O$, $CaI_2{\cdot}7H_2O$ and $CaI_2{\cdot}6.5H_2O$. *Acta Crystallogr. Sect. C. Struct. Chem.* **70**, 876–881 (2014).
38. H. Schmidt, E. Hennings, W. Voigt, Crystal structures of hydrates of simple inorganic salts. III. Water-rich aluminium halide hydrates: $AlCl_3{\cdot}15H_2O$, $AlBr_3{\cdot}15H_2O$, $AlI_3{\cdot}15H_2O$, $AlI_3{\cdot}17H_2O$ and $AlBr_3{\cdot}9H_2O$. *Acta Crystallogr. Sect. C. Struct. Chem.* **70**, 882–888 (2014).
39. A. Fortes, F. Fernandez-Alonso, M. Tucker, I. Wood, Isothermal equation of state and high-pressure phase transitions of synthetic meridianiite ($MgSO_4{\cdot}11D_2O$) determined by neutron powder diffraction and quasielastic neutron spectroscopy. *Acta Crystallogr. Sect. B Struct. Sci. Cryst. Eng. Mater.* **73**, 33–46 (2017), 10.1107/S2052520616018254.
40. J. F. L. Hausmann, *Handbuch der Mineralogie* (Vol. **3**. Vandenhoeck und Ruprecht, 1847).
41. G. M. Marion, A theoretical evaluation of mineral stability in Don Juan Pond, Wright Valley, Victoria Land. *Antarct. Sci.* **9**, 92–99 (1997).
42. R. V. Gough *et al.*, Brine formation via deliquescence by salts found near Don Juan Pond, Antarctica: Laboratory experiments and field observational results. *Earth Planet. Sci. Lett.* **476**, 189–198 (2017).
43. J.-A. Hernandez, R. Caracas, S. Labrosse, Solubility of salt in dense high-temperature ice suggests electrolyte permeability in mantles of water-rich exoplanets. *Nat. Commun.* **13**, 3303 (2022).
44. B. Journaux *et al.*, Salt partitioning between water and high-pressure ices. Implication for the dynamics and habitability of icy moons and water-rich planetary bodies. *Earth Planet. Sci. Lett.* **463**, 36–47 (2017).
45. S. Klotz, L. Bove, T. Strässle, T. Hansen, A. Saitta, The preparation and structure of salty ice VII under pressure. *Nat. Mater.* **8**, 405–409 (2009).
46. S. D. Vance *et al.*, Geophysical investigations of habitability in ice-covered ocean worlds: Geophysical habitability. *J. Geophys. Res. Planets* **123**, 180–205 (2018).
47. S. M. Howell, R. T. Pappalardo, Band formation and ocean-surface interaction on Europa and Ganymede. *Geophys. Res. Lett.* **45**, 4701–4709 (2018).
48. R. T. Pappalardo *et al.*, Science potential from a Europa lander. *Astrobiology* **13**, 740–773 (2013).
49. S. M. MacKenzie *et al.*, The Enceladus Orbilander mission concept: Balancing return and resources in the search for life. *Planet. Sci. J.* **2**, 77 (2021).
50. K. Kalousová, C. Sotin, Melting in high-pressure ice layers of large ocean worlds–implications for volatiles transport. *Geophys. Res. Lett.* **45**, 8096–8103 (2018).
51. B. Journaux, Salty ice and the dilemma of ocean exoplanet habitability. *Nat. Commun.* **13**, 3304 (2022).
52. J. Dalton *et al.*, Chemical composition of icy satellite surfaces. *Space Sci. Rev.* **153**, 113–154 (2010).
53. R. Carlson, W. Calvin, J. Dalton, "Europa's surface composition" in *Europa* (University of Arizona Press, Tucson, 2009), pp. 283–327.
54. C. Prescher, V. B. Prakapenka, DIOPTAS: A program for reduction of two-dimensional X-ray diffraction data and data exploration. *High Press. Res.* **35**, 223–230 (2015).
55. N. Holtgrewe, E. Greenberg, C. Prescher, V. B. Prakapenka, A. F. Goncharov, Advanced integrated optical spectroscopy system for diamond anvil cell studies at GSECARS. *High Press. Res.* **39**, 457–470 (2019).
56. I. Kantor *et al.*, BX90: A new diamond anvil cell design for X-ray diffraction and optical measurements. *Rev. Sci. Instrum.* **83**, 125102 (2012).